DATA EFFICIENT IMPLEMENTATION OF UWBWA SAR ALGORITHMS

Richard Rau and James H. McClellan

Center for Signal and Image Processing
School of Electrical and Computer Engineering
Georgia Institute of Technology
Atlanta, Georgia 30332–0250, USA
james.mcclellan@ece.gatech.edu

ABSTRACT

It is shown that the particular form of the frequency support of raw data and focused imagery obtained from an ultra-wideband, wide beamwidth synthetic aperture radar system can be exploited in non-separable sampling schemes to reduce the overall amount of raw data samples and image pixels that need to be stored and computed. Furthermore, it is demonstrated that the constant integration angle backprojection (CIAB) image former implicitly applies a fan filter that interpolates raw data sampled on a quincunx grid back onto the underlying rectangular grid. This subtle property of the CIAB has not been exploited so far. It leads to higher quality images with less computational complexity.

1. INTRODUCTION

Low-frequency, wide angle, ultra-wideband (UWBWA) synthetic aperture radars (SAR) provide high slant-range and cross-range resolution and can penetrate foliage and soil to detect obscured targets. Although UWBWA SARs do not differ structurally from other strip-map SARs, their wide beamwidth and large fractional bandwidth require a careful investigation of their new properties [2].

For example the frequency support of UWBWA raw data and of focused UWBWA SAR images is quite different from that of narrow angle, narrow-band systems. As a consequence the sampling schemes commonly used for SAR data lead to a redundant signal representation in the case of UWBWA SAR data. Non-separable sampling techniques allow to remove those redundancies and lead to more efficient implementations of processing algorithms for UWBWA SAR data.

2. STRIP MAP SAR

We consider here the 2-D slant-plane geometry for strip map SAR with the radar and the illuminated area in the same plane (see Fig. 1) [4]. The radar is moved along the x-axis. At regular intervals the antenna emits a bandlimited radar pulse $p(t)$ and records all returns reflected by the targets within the antenna footprint as a 1-D signal $d(x,t)$, where x is the radar location and t denotes fast-time. The

This work was prepared through collaborative participation in the Advanced Sensors Consortium sponsored by the U.S. Army Research Laboratories under cooperative agreement DAAL01-96-2-0001.

It was also supported by the Joint Services Electronics Program under contract DAAH-04-96-1-0161.

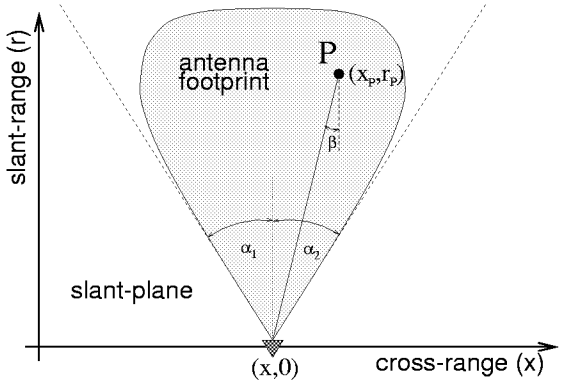

Figure 1: Data collection geometry for strip map SAR.

radar pulse is specified by its fractional bandwidth

$$BW_f = 2\frac{\omega_{\max} - \omega_{\min}}{\omega_{\max} + \omega_{\min}} \tag{1}$$

where $\omega_{\min}$ and $\omega_{\max}$ are the lower and upper cutoff frequencies of $p(t)$. We consider here UWBWA SAR systems that have a fractional bandwidth close to its maximum value of 2. The beamwidth and squint of the antenna can be specified by the two angles α_1 and α_2 in Fig. 1.

Point P in Fig. 1 denotes an arbitrary reflector. The transmitted pulse reaches point P under the aspect angle β. While the radar platform passes the scatterer P, its distance to the scatterer and, hence, the round-trip delay of the radar pulse $p(t)$ changes in a hyperbolic fashion. Due to this underlying hyperbolic structure of the recorded 2-D raw data $d(x,t)$, the region of support Ω_D of its Fourier transform $D(k_x,\omega)$ has the form shown in Fig. 2a [4, 3]. It is bandlimited in ω by $\omega_{\min}$ and $\omega_{\max}$, respectively. In k_x it is bandlimited by the ω dependent straight lines $k_x = \frac{2}{c}\omega \sin\alpha_1$ and $k_x = \frac{2}{c}\omega \sin\alpha_2$, where c denotes the speed of light. Most SAR systems use narrow beamwidths and radar pulses with a small BW_f. In this case, Ω_D consists of two almost square patches. This type of raw data is discretized in three steps. First it is frequency-shifted such that one of the patches is centered at the origin (called baseband transformation). Then the second patch is removed by lowpass filtering. The resulting signal is a complex lowpass signal and can be sampled in x and t in a separable fashion on a rectangular grid. On the other hand, for UWBWA SARs with $BW_f \approx 2\,\Omega_D$ is fan shaped and extends almost all the way to the origin. A baseband

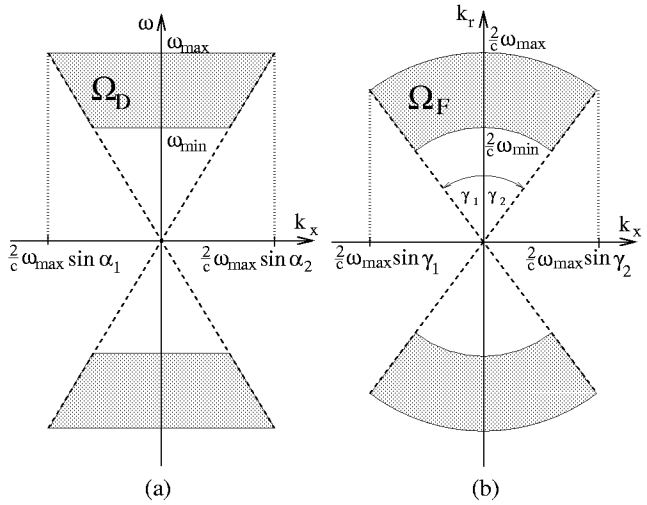

Figure 2: (a) Frequency support of raw data. (b) Frequency support of focused image.

transformation is not performed. Usually the signal is directly sampled on a rectangular grid, but this paper exploits the fact that this signal representation is redundant.

After data collection the raw data is focused to remove the hyperbolic spread of target information. A wide variety of different imaging algorithms exist [4]. In [3], it was demonstrated that the constant integration angle backprojector (CIAB) has some interesting properties. In this paper we extend these results by showing that the CIAB performs implicitly a 2-D filtering operation that can be exploited. The constant integration angle backprojector correlates $d(x,t)$ with hyperbolas over a finite aperture

$$f(x,r) = \int\int \hat{t}^2 d(\hat{x},\hat{t}) \frac{1}{r} w\left(\frac{\hat{x}-x}{r}\right) \delta\left(\hat{t} - \frac{2}{c}\sqrt{(\hat{x}-x)^2+r^2}\right) d\hat{x}d\hat{t} \quad (2)$$

The length and shape of the aperture is completely specified by its weighting function $w(\cdot)$. The CIAB in (2) is not applicable to baseband transformed raw data without modifications. The ROS of $w(\cdot)$ is given as $\Omega_w = [\tan\gamma_1, \tan\gamma_2]$, where $[\gamma_1, \gamma_2]$ is the interval of aspect angles over which target returns are coherently integrated. In UWBWA SAR systems the integration angle $\gamma = \gamma_2 - \gamma_1$ can be $90°$ or more. The ROS Ω_F of $F(k_x, k_r)$ is shown in Fig. 2b [4, 3]. It has the form of a wedge shaped ring segment. The inner and outer radii of the ring are $\frac{2}{c}\omega_{\min}$ and $\frac{2}{c}\omega_{\max}$, respectively. The wedge shaped area is limited by the two straight lines $k_x = k_r \tan\gamma_1$ and $k_x = k_r \tan\gamma_2$. Similarly to the raw data domain, separable sampling of $f(x,r)$ does not exploit the particular shape of Ω_F and can be quite redundant.

3. SAMPLING WITH GENERAL SAMPLING GEOMETRIES

We borrow here the notation and terminology for general multidimensional sampling from [1]. Let us consider a 2-D continuous signal $x_a(t_1,t_2) = x_a(\mathbf{t})$, where $\mathbf{t} = (t_1,t_2)^T \in \mathbf{R}^2$. A general sampling lattice can be defined by choosing two linearly independent vectors. We concatenate them into a sampling matrix $\underline{\mathbf{V}}$ such that the sampled signal is $x(\mathbf{n}) = x_a(\underline{\mathbf{V}}\mathbf{n})$ with $\mathbf{n} = (n_1,n_2)^T \in \mathbf{Z}^2$. The density ρ of sample points per unit area is given as [5]

$$\rho = \frac{1}{|\det \underline{\mathbf{V}}|} \quad (3)$$

The Fourier transform of $x(\mathbf{n})$ depends on the Fourier transform of the underlying $x_a(\mathbf{t})$ in the following fashion [1]

$$X(\underline{\mathbf{V}}^T\tilde{\boldsymbol{\omega}}) = \frac{1}{|\det \underline{\mathbf{V}}|} \sum_{\mathbf{k}} X_a(\tilde{\boldsymbol{\omega}} - \underline{\mathbf{U}}\mathbf{k})) \quad (4)$$

with $\underline{\mathbf{U}} = 2\pi\underline{\mathbf{V}}^{-T}$. The Fourier transform $X(\underline{\mathbf{V}}^T\tilde{\boldsymbol{\omega}})$ is periodic in $\tilde{\boldsymbol{\omega}}$ with the periodicity matrix $\underline{\mathbf{U}}$, i.e.

$$X(\underline{\mathbf{V}}^T(\tilde{\boldsymbol{\omega}} + \underline{\mathbf{U}}\mathbf{k})) = X(\underline{\mathbf{V}}^T\tilde{\boldsymbol{\omega}} + 2\pi\mathbf{k})) = X(\underline{\mathbf{V}}^T\tilde{\boldsymbol{\omega}}) \quad (5)$$

To find the most efficient sampling scheme for a 2-D signal you have to find a periodicity matrix $\underline{\mathbf{U}}$ such that no aliasing occurs in (4) and ρ in (3) is minimized. This approach will be used in the following two sections to determine efficient sampling schemes for the raw data $d(x,t)$ and for focused images $f(x,r)$ of UWBWA SAR systems.

Once a continuous signal has been sampled, it can be further decimated onto a sublattice of the original sampling lattice. The sublattice can again be specified by a sampling matrix $\underline{\mathbf{M}}$. The subsampled signal is then $x_s(\mathbf{n}) = x(\underline{\mathbf{M}}\mathbf{n}) = x_a(\underline{\mathbf{V}}\,\underline{\mathbf{M}}\mathbf{n})$. If $x(\mathbf{n})$ is subsampled without aliasing, $x(\mathbf{n})$ can be reconstructed from $x_s(\mathbf{n})$ by using the following two steps:

1. Expand $x_s(\mathbf{n})$ onto the original lattice of $x(\mathbf{n})$ by inserting zeros. The resulting signal is [5]

$$\tilde{x}(\mathbf{n}) = \begin{cases} x_s(\underline{\mathbf{M}}^{-1}\mathbf{n}) & \text{if } \mathbf{n} = \underline{\mathbf{M}}\mathbf{k} \text{ for some } \mathbf{k} \in \mathbf{Z}^2 \\ 0 & \text{otherwise} \end{cases}$$

2. Filter $\tilde{x}(\mathbf{n})$ with a filter that is 1 within Ω_X and 0 outside.

This reconstruction scheme will be exploited in Section 6.

4. SAMPLING THE RAW DATA

The Nyquist sampling rates for sampling the raw data (Fig. 2a) on a rectangular grid are $k_N = \frac{4}{c}\omega_{\max}\max\{|\sin\alpha_1|, |\sin\alpha_2|\}$ and $\omega_N = 2\omega_{\max}$. The resulting sampling density is $\rho = \frac{1}{4\pi^2}k_N\omega_N$. Rectangular sampling does not exploit the fan shape of Ω_D discussed in Section 2 and leads to a redundant signal representation. An alternative aliasing free periodic extension of Ω_D can be obtained with a periodicity matrix $\underline{\mathbf{U}}_2$ of the form [3]

$$\underline{\mathbf{U}}_2 = \frac{1}{2}\begin{pmatrix} k_N & -k_N \\ \omega_N & \omega_N \end{pmatrix} \quad (6)$$

In this case, the sampling density is $\rho = \frac{1}{8\pi^2}k_N\omega_N$. Thus, the corresponding sampling scheme requires only half as many samples as for rectangular sampling. The two sampling schemes have a useful relationship. The sampling matrix $\underline{\mathbf{V}}_2$ can be written as a product of two sampling matrices

$$\underline{\mathbf{V}}_2 = 2\pi\begin{pmatrix} \frac{1}{k_N} & \frac{-1}{k_N} \\ \frac{1}{\omega_N} & \frac{1}{\omega_N} \end{pmatrix} = 2\pi\begin{pmatrix} \frac{1}{k_N} & 0 \\ 0 & \frac{1}{\omega_N} \end{pmatrix}\begin{pmatrix} 1 & -1 \\ 1 & 1 \end{pmatrix} \quad (7)$$

The first matrix is the sampling matrix $\underline{\mathbf{V}}_1$ for the rectangular sampling. The second matrix defines the quincunx sublattice of the rectangular sampling grid (see Fig. 3b) [5]. Thus, the data can first be sampled onto the rectangular grid and in case data reduction is needed can be subsampled onto the quincunx grid. The effect of quincunx sampling on Ω_D and Ω_F will be illustrated in the next section.

5. SAMPLING UWBWA SAR IMAGES

While the relationship between rectangular sampling and data efficient sampling for $d(x,t)$ does not depend on particular system properties, efficient sampling for UWBWA SAR images is more complicated. For the following investigation we assume that $\gamma_2 = -\gamma_1$. It was shown in [3] that the following three periodicity matrices lead to aliasing free periodic extensions of Ω_F

$$\underline{\mathbf{U}}_1 = k_{N_r} \begin{pmatrix} \sin\frac{\gamma}{2} & 0 \\ 0 & 1 \end{pmatrix} \tag{8}$$

$$\underline{\mathbf{U}}_2 = \frac{1}{2} k_{N_r} \begin{pmatrix} \tan\frac{\gamma}{2} & -\tan\frac{\gamma}{2} \\ 1 & 1 \end{pmatrix} \tag{9}$$

$$\underline{\mathbf{U}}_3 = \frac{1}{2} k_{N_r} \begin{pmatrix} 1 & 1 \\ \sqrt{3} & -\sqrt{3} \end{pmatrix} \tag{10}$$

where $\gamma = \gamma_2 - \gamma_1$ is the integration angle and $k_{N_r} = \frac{4}{c}\omega_{\max}$. The matrix $\underline{\mathbf{U}}_1$ defines again a separable rectangular sampling grid. The sampling defined by $\underline{\mathbf{U}}_2$ and $\underline{\mathbf{U}}_3$ are structurally very similar. Both $\underline{\mathbf{V}}_2$ and $\underline{\mathbf{V}}_3$ can be written in the factored form (7), i.e. as the product of a rectangular sampling matrix followed by a quincunx subsampling matrix. The periodic extension of Ω_F by $\underline{\mathbf{U}}_2$ is shown in Fig. 3a. In the following we refer to the sampling defined by $\underline{\mathbf{U}}_2$ as quincunx sampling and the one defined by $\underline{\mathbf{U}}_3$ as hexagonal sampling, because each grid point has six nearest neighbors sitting on the corners of a hexagon [5]. These three sampling schemes have the following sampling densities

$$\rho_1 = \frac{1}{\pi^2} k_{N_r}^2 \sin\frac{\gamma}{2} \quad \rho_2 = \frac{1}{2\pi^2} k_{N_r}^2 \tan\frac{\gamma}{2} \quad \rho_3 = \frac{\sqrt{3}}{2\pi^2} k_{N_r}^2 \tag{11}$$

The sampling scheme with the least amount of redundancy is the one with the smallest sampling density. Figure 4a shows ρ_1, ρ_2 and ρ_3 as functions of γ. The three curves intersect for $\gamma = 120°$. If the integration angle γ is smaller than $120°$, quincunx sampling is more efficient than rectangular sampling. On the other hand hexagonal sampling is more efficient than rectangular sampling for $\gamma > 120°$. Using efficient non-separable sampling can lead to considerable data reduction. For example for $\gamma = 90°$ the ratio $\frac{\rho_2}{\rho_1} = \frac{1}{\sqrt{2}} \approx 0.7$, i.e. about 30% less image pixels need to be computed without losing any image information.

6. DATA EFFICIENT IMPLEMENTATION OF CIAB

In this section we will show how non-separable sampling in the raw data and the image domain can be efficiently incorporated into the CIAB to reduce overall computation and data storage.

Most existing implementations of the CIAB expect rectangularly sampled raw data and produce rectangularly sampled images. It was shown in the previous section that optimal sampling in the image domain can be realized as rectangular sampling followed by quincunx subsampling. Since the CIAB computes each image pixel independently, the optimal sampling scheme can easily be incorporated into the CIAB by computing only the points on the quincunx sublattice of the rectangular sampling grid. This requires minor changes in the software and leads to an immediate reduction in computational complexity. If the image is needed on a rectangular grid, the two step procedure of Section 3 can be used to generate it.

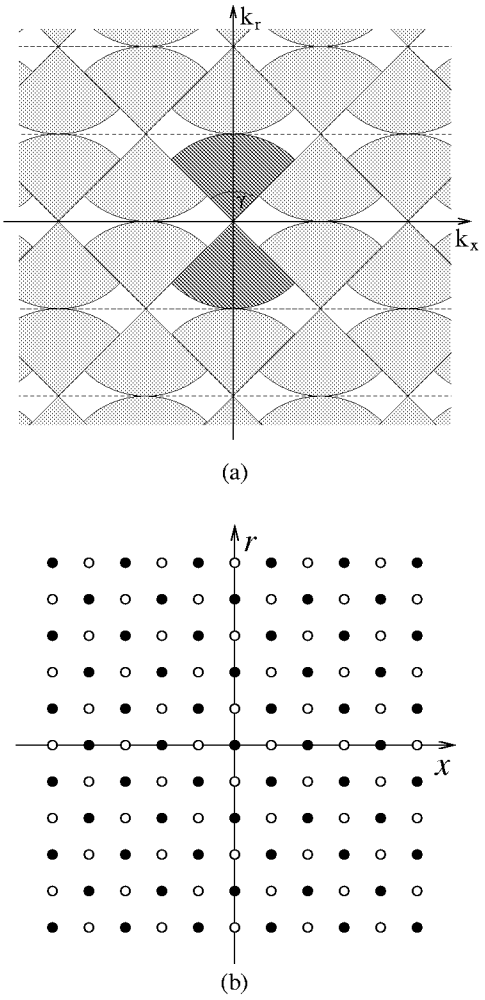

Figure 3: (a) Periodic extension of Ω_F by quincunx sampling. (b) Quincunx sublattice (dark dots) and quincunx co-lattice (empty dots) of rectangular sampling grid.

To exploit the efficient sampling of the raw data without complicating the computations in the CIAB, the raw data samples need to be interpolated from the qincunx sublattice onto the underlying rectangular grid (see Section 3). First the raw data is expanded onto the rectangular grid and the quincunx co-lattice is set to zero. This requires no computations. The structure of the resulting signal $\hat{d}(k\Delta\hat{x}, l\Delta t)$ is the one of Fig. 3b with data values marked as dark dots and zeros as empty dots. Then $\hat{d}(k\Delta\hat{x}, l\Delta t)$ needs to be filtered with a fan shaped filter to remove the shifted spectral copy of the signal.

This operation can, however, be avoided. The Fourier transform of the image $F(k_x, k_r)$ can be written as an inner product in ω of

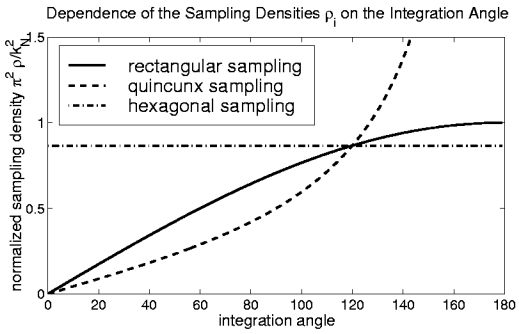

Figure 4: Sampling densities for sampling schemes defined by $\underline{\mathbf{U}}_1$, $\underline{\mathbf{U}}_2$ and $\underline{\mathbf{U}}_3$.

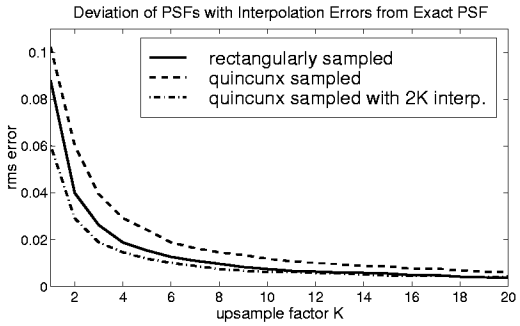

Figure 5: RMS error of the image of an ideal point scatterer focused from rectangularly and efficiently sampled raw data as a function of the upsampling factor K.

$D(k_x, \omega)$ with a 3-D kernel $K(k_x, \omega, k_r)$, .i.e

$$F(k_x, k_r) = \int_{-\infty}^{\infty} D^*(k_x, \omega) K(k_x, \omega, k_r) d\omega \qquad (12)$$

In [3] the kernel was shown to have the property: $K(k_x, \omega, k_r) \approx 0$ for $|k_x| \geq \left|\frac{2}{c}\omega \sin\frac{\gamma}{2}\right|$. Hence, the CIAB suppresses all frequency components of $D(k_x, \omega)$ outside of a fan shaped area. It performs implicitly the fan filtering of $\hat{d}(k\Delta\hat{x}, l\Delta t)$ needed for interpolating the signal onto the rectangular grid, if $\max\{|\alpha_1|, |\alpha_2|\} \geq \frac{\gamma}{2}$. An explicit interpolation filter is not necessary. As a consequence quincunx sampled raw data can be used with the CIAB without additional computation.

Some degradations of the image quality can, however, arise due to 1-D fast-time interpolation required in any implementation of the CIAB. A computer implementation of the CIAB is based on the following discretized version of (2)

$$f(n\Delta x, m\Delta r) = \frac{1}{m\Delta r} \sum_k \left((k\Delta\hat{x} - n\Delta x)^2 + (m\Delta r)^2\right)$$
$$d\left(k\Delta\hat{x}, \frac{2}{c}\sqrt{(k\Delta\hat{x} - n\Delta x)^2 + (m\Delta r)^2}\right) w\left(\frac{k\Delta\hat{x} - n\Delta x}{m\Delta r}\right) \qquad (13)$$

Equation (13) requires raw data values sampled on a uniform grid in cross-range and at non-uniformly spaced sample locations in fast-time. Since the available raw data $d(k\Delta\hat{x}, l\Delta t)$ is discrete in cross-range and fast-time, 1-D interpolation is necessary with respect to fast-time before the data can be summed coherently. To obtain computationally efficient implementations the interpolation schemes are not ideal and errors are introduced in the formed image. These errors tend to be larger, if $\hat{d}(k\Delta\hat{x}, l\Delta t)$ is used in (13) instead of $d(k\Delta\hat{x}, l\Delta t)$. This effect can, however, be compensated by exploiting the particular structure of $\hat{d}(k\Delta\hat{x}, l\Delta t)$. The signal $\hat{d}(k\Delta\hat{x}, l\Delta t)$ is zero at every other grid point (see Fig. 3b). This reduces the number of computations for a 1-D FIR interpolation filter by 50%, or equivalently better interpolation can be used without increasing the computational complexity. Improving interpolation leads to smaller degradations in the focused images.

7. NUMERICAL RESULTS

Experiments were conducted to confirm these theoretic results. For the 1-D interpolation in the CIAB the raw data was interpolated first in fast-time onto a K times finer grid and then nearest neighbor interpolation was performed. Obviously, the larger K is, the smaller are the interpolation errors. If the raw data is $\hat{d}(k\Delta\hat{x}, l\Delta t)$, K can be doubled compared to $d(k\Delta\hat{x}, l\Delta t)$ without increasing the computational complexity. The quality of a formed image was measured with the rms error between the image and an image formed using interpolation with $K = 100$. Raw data was synthesized for a point target at $r = 75$m imaged with a pulsed UWBWA SAR. The pulse has an upper cutoff frequency of about 900MHZ and a bandwidth of approximately 800MHz. The antenna beam was chosen to be von Hann shaped with a width of 100°. The raw data was sampled in fast-time with $\Delta t = 0.5$ns and in cross-range with $\Delta x = 9.75$cm. This data was then subsampled on the quincunx sublattice to obtain a data efficient representation. The CIAB was set to focus the raw data over an integration angle of $\gamma = 90°$ with $w(\cdot)$ in (13) being a rectangular window. Figure 5 shows the rms errors for the rectangularly and quincunx sampled raw data as a function of K as well as for the quincunx sampled data processed with $2K$ in the interpolation.

In summary exploiting the particular structure of UWBWA SAR raw data and images leads to an implementation of the CIAB that is more efficient with respect to both computation and data storage. For $\gamma = 90°$, the number of computed image pixels is reduced by 30%. Furthermore, the amount of raw data storage is reduced by 50% compared to traditional sampling and the rms error of the formed images is smaller for the same amount of computation per image pixel.

8. REFERENCES

[1] D. E. Dudgeon and R. M. Mersereau. *Multidimensional Digital Signal Processing*. Prentice Hall, Englewood Cliffs, NJ, 1984.

[2] R. Goodman, S. Tummala, and W. Carrara. Issues in ultra-wideband, widebeam sar image formation. In *Proceedings of the 1995 IEEE National Radar Conference*, pages 479–485, 1995.

[3] R. Rau. *Postprocessing Tools for Ultra-wideband SAR Images*. PhD thesis, Georgia Institute of Technology, 1998.

[4] M. Soumekh. *Fourier Array Imaging*. Prentice Hall, Englewood Cliffs, NJ, 1994.

[5] P. P. Vaidyanathan. *Multirate Systems and Filter Banks*. Prentice Hall, Englewood Cliffs, NJ, 1993.